Low-energy photoelectron interference structure in attosecond streaking

JINTAI LIANG,[1] YUEMING ZHOU,[1,4] JIA TAN,[1] MINGRUI HE,[1] QINGHUA KE,[1] YONG ZHAO,[1] MIN LI,[1] WEICHAO JIANG,[2,5] (iD) **AND PEIXIANG LU[1,3,6]**

[1]*Wuhan National Laboratory for Optoelectronics and School of Physics, Huazhong University of Science and Technology, Wuhan 430074, China*
[2]*College of Physics And Optoelectronic Engineering, Shenzhen University, Shenzhen 518060, China*
[3]*Hubei Key Laboratory of Optical Information and Pattern Recognition, Wuhan Institute of Technology, Wuhan 430205, China*
[4]*zhouymhust@hust.edu.cn*
[5]*jiang.wei.chao@szu.edu.cn*
[6]*lupeixiang@hust.edu.cn*

Abstract: By numerically solving the time-dependent Schrödinger equation, we theoretically investigate the dynamics of the low-energy photoelectrons ionized by a single attosecond pulse in the presence of an infrared laser field. The obtained photoelectron momentum distributions exhibit complicated interference structures. With the semiclassical model, the originations for the different types of the interference structures are unambiguously identified. Moreover, by changing the time delay between the attosecond pulse and the infrared laser field, these interferences could be selectively enhanced or suppressed. This enables us to extract information about the ionization dynamics encoded in the interference structures. As an example, we show that the phase of the electron wave-packets ionized by the linearly and circularly polarized attosecond pulses can be extracted from the interference structures of the direct and the near-forward rescattering electrons.

1. Introduction

The advent of attosecond pulses provides a powerful tool for investigating atomical and molecular dynamics on their natural time scale. Attosecond streaking, which is based on an attosecond pulse serving as the pump pulse and a phase controlled infrared (IR) field as the probe pulse, is an extensively used technique. It is initially proposed to characterize the attosecond pulses as well as the IR field [1–3]. This technique has been also demonstrated to be very useful for tracing and controlling the attosecond electron dynamics in atoms and molecules. In attosecond streaking scheme, the electrons are released by the attosecond pulses and accelerated by the moderate IR laser field. The photoelectron momentum distributions (PEMDs) are shifted by the amount of momentum transferred from the IR field to the continuum electron wave packets (EWPs). Thus, the time information is mapped onto the energy axis of photoelectrons with attosecond precision. The first proof-of-principle implementation is the measurement on the time delay of the atomic photoemission from Neon [4]. These observations have triggered a large number of theoretical investigations of time delay in atomic [5–12] and molecular photoionization [13–15], and photoemission from the solid surface [16–19]. In addition, the feasibility of observing the buildup of the Fano resonance in time domain with attosecond streaking technique has been proved [20–23]. Moreover, the streaking spectrum also encodes information of the electron wave-packets ionized by the attosecond pulses. The streaking technique has also been employed to retrieve the quantum phase information and the phase variation in atomic and molecular ionization [24,25].

In these attosecond streaking experiments, the photon-energy of the attosecond pulse is much higher than the electronic binding potential. The relatively weak IR field only leads to a momentum shift in the PEMDs along the laser polarization direction. For the ionization near threshold, the energy transfer of the low-energy electron is sensitive to the binding potential. Thus, by analyzing the low-energy photoelectron spectrum in the attosecond streaking, the effective binding potential can be extracted [26]. For the photoelectrons with further lower energy in attosecond streaking, they can even be driven back by the IR field and scatter with the parent ions. We should mention that in strong-field ionization by the IR field, electron-ion rescattering is an essential process and it could result in various interesting phenomena [27], such as high-order harmonic generation [28–32], high-order above-threshold ionization [33,34], nonsequential double ionization [35–37] and frustrated tunneling ionization [38,39]. The application of this rescattering process has been deeply explored. For example, the rescattering induced high-order harmonics could be used to generate attosecond pulses [40–42]. Moreover, the rescattering electrons and the resultant photons encode the structural and dynamical information of the parent ion, and thus it has been used to probe atomic and molecular structures and dynamics [43,44]. Fantastically, the rescattering electrons can interfere with the direct electrons in PEMDs, which is referred as strong-field photoelectron holography (SFPH) [45]. This SFPH is expected to be a powerful tool to probe the ultrafast electronic dynamics in atoms and molecules and it has attracted particular interests during the past years [46–49]. In our pervious works, we have demonstrated that the phase of the scattering amplitude can be extracted by the SFPH [50]. More interestingly, we have shown that the charge migration in molecules can be directly visualized by analyzing the SFPH structure [51]. Recently, we demonstrate that the ionization time [52] and the initial momentum of tunneling [53–55] can be probed using SFPH.

In this paper, we focus on the rescattering process in the scheme of attosecond streaking. Here, the rescattering photoelectron is generated by the attosecond pulse through single-photon ionization and it is driven back to the parent ion by the infrared pulse. Different from the rescattering process in strong-field tunneling ionization by the IR field, the creation and the acceleration of the photoelectron are decoupled in attosecond streaking. Thus the ionization and the rescattering processes can be separately controlled. In the past decades, these rescattering electrons and their interference have drawn considerable attention. In the case of attosecond pulse trains, the laser-induced coherent electron scattering has been experimentally observed in the PEMDs [56]. This controlled and coherent scattering enables the time resolved measurements with very high spatial resolution. For the single attosecond pulse (SAP), the rescattering process has also been theoretically studied and its dependence on the strength and wavelength of the IR driven field has been explored [57,58]. Very recently, it has been shown that backward rescattering can be controlled by changing the time delay between the SAP and the IR pulse [59]. It is well known that these rescattered electrons deliver rich information of the atomic and molecular structures and dynamics. Thus, investigations on the rescattering electron in the attosecond streaking scheme, in particularly the interference structures originating from the rescattering electrons, could open a door for time-resolved holographic imaging of the ultrafast electronic dynamics in atoms and molecules.

In this work, we study the interference structures in the PEMD produced by the SAP in the presence of an IR field by numerically solving the time dependent Schrödinger equation. We observe six types of interference structures in the PEMDs. Using the semiclassical model, we show that these structures result from the interference of the direct electrons and different types of the rescattering electrons. The originations of each type of the interference structures are unambiguously identified. Furthermore, we demonstrate that the interference structures could be selectively enhanced or suppressed by changing the time delay between the SAP and the IR field. This enables us to extract information of electrons from the specific interference structures. As an example of the application of interference in attosecond streaking, we show that the interference

of the direct and the near-forward rescattering electrons can be used to retrieve the phase of continuum EWPs ionized by the linearly and circularly polarized attosecond pulses.

2. Theoretical method

2.1. Numerically solving TDSE

We obtain the PEMDs by numerically solving the two-dimensional (2D) TDSE [60,61]. The TDSE with the single-active-electron (SAE) approximation in the length gauge is given by (atomic unites are used unless otherwise stated)

$$i\frac{\partial \Psi(\mathbf{r},t)}{\partial t} = \left[-\frac{\nabla^2}{2} + V(\mathbf{r}) - \mathbf{r}\cdot\mathbf{E}(t)\right]\Psi(\mathbf{r},t), \tag{1}$$

where $V(\mathbf{r}) = -(x^2 + y^2 + a^2)^{-1/2}$ is the effective soft-core potential. The soft-core parameters are chosen to match the ionization potential of the targets. In our work, we choose two different values $a = 0.256$ and $a = 0.85$ and the corresponding ground-state energies are $I_p = -0.9$ a.u. and $I_p = -0.48$ a.u., respectively.

The electric field $\mathbf{E}$ is written as

$$\mathbf{E}(t) = \mathbf{E}_{IR}(t) + \mathbf{E}_{SAP}(t + \tau), \tag{2}$$

where $\mathbf{E}_{IR}(t) = E_{IR}f_1(t)\cos(\omega_1 t)\mathbf{e_x}$ is the electric field of the IR pulse. E_{IR} and ω_1 are the amplitude of electric field and center frequency of the IR pulse, respectively. $f_1(t)$ is the envelope of the IR field, and it has a trapezoidal shape which rises linearly during a half cycle, then keeps constant for two cycles and decreases linearly during the last a half cycle. In our simulation, the wavelength of the IR field is 1600 nm. The intensity of the IR field is chosen to be weak so that the ionization from ground state by the IR field could be neglected. $\mathbf{E}_{SAP}(t + \tau)$ is the electric field of the SAP. In our work, we consider both linearly and circularly polarized SAP. For the circularly polarized SAP, the electric field is written as

$$\mathbf{E}_{SAP}(t + \tau) = E_{SAP}f_2(t + \tau)\left(\cos[\omega_2(t + \tau)]\frac{1}{\sqrt{1 + \eta^2}}\mathbf{e_x} + \sin[\omega_2(t + \tau)]\frac{\eta}{\sqrt{1 + \eta^2}}\mathbf{e_y}\right). \tag{3}$$

E_{SAP} and ω_2 are the amplitude of electric field and center frequency of the SAP, respectively. η is the ellipticity with $\eta = 1$ and $\eta = -1$ representing the right- and left-hand circularly polarized SAP. τ is the time delay between the IR field and the SAP. $f_2(t)$ is the envelope of the SAP. For the linearly polarized SAP, the electric field is written as

$$\mathbf{E}_{SAP}(t + \tau) = E_{SAP}f_2(t + \tau)\left(\cos[\omega_2(t + \tau)]\cos\theta\mathbf{e_x} + \cos[\omega_2(t + \tau)]\sin\theta\mathbf{e_y}\right). \tag{4}$$

θ is the angle between the $x-$axis and the polarization direction of the SAP. In this work, the envelope of the SAP is chosen as a sin-square shape lasting six cycles. The intensity of the SAP is 2×10^{14} W/cm^2.

In our simulation, we numerically solve TDSE using the split-operator spectral method [62] on a Cartesian grid ranging from -600 to 600 a.u.. The time step is fixed at $\Delta t = 0.05$ a.u. and the spatial discretization is $\Delta x = \Delta y = 0.2$ a.u.. The initial wavefunction is prepared by imaginary-time propagation [63].

2.2. The semiclassical model

We employ the semiclassical model within the strong field approximation [59] to investigate the originations of the interference structures exhibited in the PEMDs. In the attosecond streaking scheme, the continuum EWPs is created by SAP and then its evolution is governed by the IR

field. Neglecting the Coulomb interaction, the motion of the EWPs in the IR field is determined by Newtonian equation

$$\frac{d\mathbf{p}(t)}{dt} = -\mathbf{E}_{IR}(t). \tag{5}$$

In our calculation, the electron wave packet was launched by the SAP during the flat top of the trapezoidal IR pulse. Thus, the subsequent dynamic of the electron wave packet in the IR field could be described by considering the cos-like electric field: $\mathbf{E}_{IR}(t) = E_{IR}\cos(\omega t)\mathbf{e}_x$. The momentum $\mathbf{p}(t)$ and the position $\mathbf{r}(t)$ of the electron released at time t_0 are written as

$$\mathbf{p}(t) = \mathbf{A}(t) - \mathbf{A}(t_0) + \mathbf{p}_0, \tag{6}$$

and

$$\mathbf{r}(t) = \int_{t_0}^{t} \mathbf{p}(t)dt + \mathbf{r}_0, \tag{7}$$

where $\mathbf{A}(t) = -\int_{-\infty}^{t} \mathbf{E}_{IR}(t')dt' = -E_{IR}/\omega_1\sin(\omega_1 t)\mathbf{e_x}$ is the vector potential of the IR field. $\mathbf{p}_0$ and $\mathbf{r}_0$ are the initial momentum and position of the electron, respectively. It has previously been pointed out that the choice of the initial position must match the asymptotic behavior of the exact Coulomb wavefunction [7]. Here, we select the initial position as the most probable position of the electron of the respective initial quantum state [12]. In our calculation, the initial state is 1S state, thus we choose the zero as the initial position. The initial momentum is determined by the binding potential and the frequency spectrum of the SAP. The ionization time t_0 is the center of the SAP.

The low energy photoelectrons produced by the SAP could be driven back by the IR field and collide with the parent ion. Thus, there are two types of the electrons, i.e., the direct and the rescattering electrons. The direct electron reaches the detector without interaction with the parent ion after ionization. In our calculations, the vector potential of the IR field is zero as the IR field vanishes, $-\int_{-\infty}^{\infty} \mathbf{E}_{IR}(t)dt = 0$, and thus the final momentum of the direct electron is

$$\mathbf{p}_f = \mathbf{p}_0 - \mathbf{A}(t_0). \tag{8}$$

The rescattering electron is driven back by the IR pulse and rescatter with the parent ion. According to Eqs. (6) and (7), the rescattering time t_s is determined by

$$r(t_s) = \frac{E_{IR}}{\omega_1^2}\cos(\omega t_s) - \frac{E_{IR}}{\omega_1^2}\cos(\omega t_0) + [p_0 - A(t_0)](t_s - t_0) = 0, \tag{9}$$

and the recollision momentum is written as

$$p_s = A(t_s) - A(t_0) + p_0. \tag{10}$$

At the instant of recollision, the rescattering electron changes its direction. Then the final momentum of the rescattering electron is written as

$$\mathbf{p}_f = [p_s\cos\theta_0 - A(t_s)]\mathbf{e}_x + p_s\sin\theta_0\mathbf{e}_y. \tag{11}$$

Here θ_0 is the rescattering angle. In our calculations, we consider the rescattering angle randomly distributing between 0 and 2π. Depending on the initial momentum of the photoelectron, there are more than one solution for the rescattering time t_s. In our calculation, we only consider the electrons where rescattering occurs at the first and second returnings, as sketched by types C and D in Fig. 1. Note that when the coulomb effect on the trajectory of the electron is neglected, only the electrons with the zero transverse momentum can be driven back by the IR pulse.
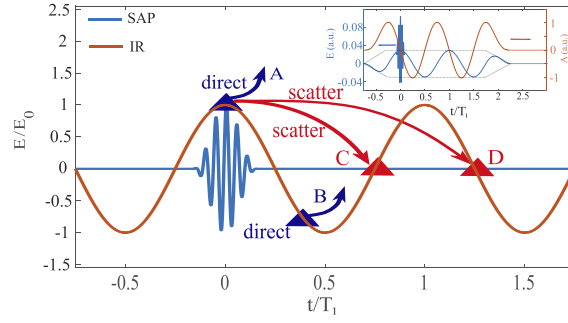
Fig. 1. Schematic illustration of interference trajectories in attosecond streaking. The blue and red lines are the electric field of the SAP and IR pulses, respectively. A represents the direct electron ionized at the center of the SAP. B is the direct electron ionized by the IR field between $0.25T_1$ and $0.5T_1$. C and D are the rescattering electrons ionized at the center of the SAP and scatter from the ion on the first and second returning, respectively. T_1 is the optical cycle of IR field. The insert shows the electric field of the laser pulse when the time delay between the SAP and IR pulse is zero. The blue and orange solid lines are the electric field and the vector potential of the laser field, respectively. The black dotted line is the envelope of the IR field.

In the semiclassical model, the interference pattern in the PEMDs could be estimated by considering the classical action along the trajectories [64,65]. Therefore, the classical actions of the direct and rescattering electrons with the final momentum $\mathbf{p}_f = p_x\mathbf{e}_x + p_y\mathbf{e}_y$ are given by

$$S_d^{SAP} = \int_{t_0}^{t} \left[\frac{p_x + A(t')}{2}\right]^2 dt' + I_p(t - t_0) + \frac{p_y^2}{2}(t - t_0), \tag{12}$$

and

$$S_s^{SAP} = \int_{t_0}^{t_s} \left[\frac{A(t') - A(t_0) + p_0}{2}\right]^2 dt' + \int_{t_s}^{t} \left[\frac{p_x + A(t')}{2}\right]^2 dt' \\ + I_p(t - t_0) + \frac{p_y^2}{2}(t - t_s), \tag{13}$$

respectively.

Due to the broad frequency spectrum of the attosecond pulse, the atom could be prompted to high excited state by the SAP. The excited state is subsequently ionized by the weak IR pulse. The phase S_d^{IR} of this type of electron is

$$S_d^{IR} = \frac{1}{2} \int_{t_i^{IR}}^{t} [p_x + A(t')]^2 dt' + I_p(t - t_i^{IR}) + \frac{p_y^2}{2}(t - t_i^{IR}), \tag{14}$$

where t_i^{IR} is the ionization time, determined by

$$\frac{1}{2}\left[p_x + A(t_i^{IR})\right]^2 + \frac{1}{2}p_y^2 + I_p = 0. \tag{15}$$

The electrons with the same final momentum via different processes interfere with each other in the PEMDs. The interference structures are given by

$$M^2(\mathbf{p}) = |M_i(\mathbf{p}) + M_j(\mathbf{p})|^2 = |M_i(\mathbf{p})|^2 + |M_j(\mathbf{p})|^2 + 2|M_i(\mathbf{p})||M_j(\mathbf{p})| \cos(S_i - S_j). \tag{16}$$

$M_i(\mathbf{p})$ and $M_j(\mathbf{p})$ represent the ionization amplitudes of the EWPs from two different processes. S_i and S_j are the corresponding phases. In our calculations, we only calculate the phase of the

different processes, which determines the shape of the interference structure in the PEMDs. Note that the semiclassical model does not consider the phase due to the rescattering process, and thus it fails in quantitative description of the interference structure. However, the overall shape predicted by this simple model is reliable [65] and it could be used to identify the originations of the different types of interference.

3. Interference structures in PEMDs

3.1. PEMDs obtained by solving TDSE

In Fig. 2, we show the PEMDs for the ionization of model He obtained by solving the 2D TDSE. The center frequencies of the SAP in Figs. 2(a) and 2(b) are 1.02 a.u. and 1.55 a.u., respectively. The 1600-nm IR pulse and SAP are both polarized along x−axis with the intensities of 6×10^{13} and 2×10^{14} W/cm^2, respectively. Here, we select He as an example to demonstrate the interference structure. The large binding potential of He ensures that the tunneling ionization from its ground state by the IR streaking field is negligibly small and could be safely neglected. The PEMDs reveal a two-lobe structure for both cases, which is the characteristic feature of the single-photon ionization from a ground state with S symmetry. The center of the two-lobe is zero due to the zero time delay (as shown in Fig. 1) between the SAP and IR pulse. Figures 2(a) and 2(b) exhibit the complex interference structures, as marked as I−VI.
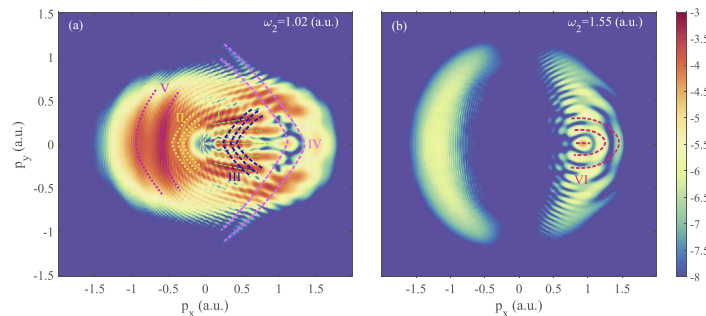

Fig. 2. PEMDs for ionization of model He atom ($I_p = -0.9$ a.u.) by numerically solving TDSE. The center frequencies of the SAP for (a) and (b) are $\omega_2 = 1.02$ a.u. and $\omega_2 = 1.55$ a.u., respectively. The intensities of the 1600-nm IR field and the SAP are 6×10^{13} W/cm^2 and 2×10^{14} W/cm^2. The time delay between the IR pulse and SAP is zero. The IR field and SAP are both polarized along the x−axis. I−VI represent six types of interference structures in the PEMDs.

The interference labeled as I displays a spiderlike structure in $p_x>0$ plane. This interference structure is similar to the holographic interference originating from the direct and the near-forward-rescattering electrons in strong-field tunneling ionization by IR or mid-infrared laser fields [45]. The interference pattern labeled as II has an arc-like structure in $p_x<0$ plane with a narrow width. Label III indicates the incoming semi-rings whose density decreases as $|p_x|$ increases, which is similar to the intracycle interference in strong field tunneling ionization [66]. The type IV fringes exhibit as outgoing semi-rings, opposed to type III. The width of the rings and the space between the rings increases as $|p_x|$ increases. This interference structure is similar to the interference between direct and the rescattering electrons launched on two successive quarters of the laser field in strong-field tunneling ionization [67]. In the relatively large momentum region, there is another type of structure labeled by V. This interference also displays as the curved rings structure, similar to type II. However, the width of the rings for type V is much larger than type II, indicating the different originations of types II and V. As the center frequency of the SAP increases, the interference patterns in PEMD become much simpler, as shown in

Fig. 2(b). Only the semi-rings interference structure in $p_x>0$ plane is visible, as labeled by VI in Fig. 2(b). These interference structures are quite different from each other, indicating that they originate from different processes.

In pervious works, the central frequency of the SAP is usually far above the ionization threshold and thus the relatively weak IR field only leads to a momentum shift in the PEMDs. While for our situation, the photon energy of the attosecond pulse is close to the ionization threshold, the electrons can be driven back by the IR field and rescatter with the parent ions. In the next section, we will identify the responsible rescattering processes for these interference structures.

3.2. Identify the originations of the interference structures

We employ the semiclassical model to analyze these interference structures in the PEMDs. As mentioned in Sec. 2.2, the EWPs created by the SAP could reach the detector through two different pathways, with (rescattering electron) and without (direct electron) a rescattering with the parent ion. Based on the scattering angles θ_0, we classify rescattering electrons into the forward ($\theta_0 \in [-\pi/2, \pi/2]$) and backward rescattering electrons ($\theta_0 \in [\pi/2, 3\pi/2]$). We calculate the phases of the direct, the forward and backward rescattering electrons with Eq. (12) and Eq. (13). The electrons could return to the parent ion many times and we calculate the electrons where rescattering occurs at the first returning in this case, as indicated by type C in Fig. 1. Figure 3(a) displays the interference between direct and the forward rescattering electrons. It exhibits the spiderlike structure and is located at the $p_x>0$ plane, which coincides with the structure labeled by I in in Fig. 2(a). Therefore, the interference structure labeled by I in Fig. 2(a) originates from the interference between the forward rescattering and the direct electrons. The interference between the backward-rescattering and the direct electrons exhibits the arc-like structure as shown in Fig. 3(b). This interference structure, which is located at the $p_x<0$ and has narrow width, has the same characteristic with the fringe labeled by II in Fig. 2(a), which means that the structure labeled by II originates from the interference between the direct and the backward rescattering electrons. These two types of interference structures are similar to the hologram in strong-field ionization. Thus, we refer to the interference structures labeled by I and II as forward and backward rescattering hologram, respectively. Note that the forward and backward rescattering electrons are classified by the scattering angle θ_0, thus the forward-rescattering and the backward-rescattering hologram connect with each other at $\theta_0 = \pi/2$, as shown in Fig. 2(a). This phenomenon is not easy to be observed in the ionization of an IR pulse due to the small differential scattering cross section for backward-rescattering electrons [67].

Due to the broad frequency spectrum of the SAP, when the central photon energy of the SAP is close to the ionization threshold, the atoms can be excited by the SAP. The weak IR field can ionize the atoms from the excited state. We calculate the phase of the electrons ionized by the IR field from the excited state with the Eq. (14). Figure 3(c) shows the interference between the electrons ionized by the IR pulse and the direct electrons ionized by the SAP. This incoming semi-rings structure, whose intensity decreases as $|p_x|$ increases, coincide with the fringes marked as III in Fig. 2(a), which means that the interference labeled by III originates from the interference between the direct electrons ionized by the IR pulse and the SAP. The interference between the electrons ionized by the IR pulse and the forward-rescattering electrons is displayed in Fig. 3(d). This interference structures exhibit the outgoing semi-rings and the space between the rings increases as $|p_x|$ increases. Comparing this semi-rings structures with the interference labeled by IV in Fig. 2(a) indicates that the type IV interference structures originate from the interference between the electrons ionized by the IR field and the forward-rescattering electrons ionized by SAP. In the pervious work, it was suggested that the interference between the electrons directly ionized from the ground state by a strong IR field and the electrons ionized by a SAP can be used to extract the carrier-envelope phase (CEP) of the attosecond pulses [68]. In these two types of
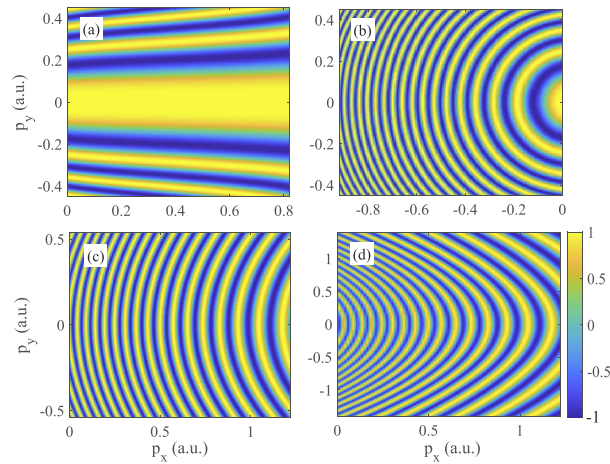
Fig. 3. Interference structures calculated by the semiclassical model. (a) and (b) show the interference between the direct electrons ionized by the SAP and the electrons rescattering with the ions at the first returning. (a) and (b) are for the forward-rescattering and backward-rescattering, respectively. (c) shows the interference between the electrons ionized from the excited state by the IR field and the direct electrons ionized by the SAP. (d) is the interference structures originating from the interference between the forward-rescattering electrons ionized by the SAP and the electrons ionized from excited state by the IR field.

interference structures, the creation and the acceleration of the EWPs are also coupled. It implies that these interference structures have potential to retrieve the CEP of the attosecond pulses.

In Fig. 4(a), we show the relationship between the final longitudinal momentum p_x and the initial momentum p_0 for the rescattering occurring at the first returning (type C, Fig. 1). The blue and the red lines correspond to the forward-rescattering and backward-rescattering electrons, respectively. Here, we calculate the rescattering angle $\theta_0 = 0°$ for forward-rescattering and $\theta_0 = \pi$ for backward-rescattering. For the forward-rescattering electron, the final momentum is located at the $p_x > 0$, and it is located at $p_x < 0$ for the backward-rescattering electron. The final momentum of the forward-rescattering electron increases monotonously with the initial momentum. Whereas for the backward-rescattering electron, the final momentum decreases first and then increases as the initial momentum increases. There are two solutions of the initial longitudinal momentum for the same final momentum and we refer to these solutions as the short and long trajectories. The backward rescattering electrons from these two trajectories can interfere with each other in PEMDs. Figure 4(c) shows this interference structure obtained with the semiclassical model. The wide curved rings structures, which are located at the relatively large momentum region in $p_x < 0$ plane, are similar to the interference structure labeled as V in Fig. 2(a), which means that the type V structures originate from the interference between the backward-rescattering electrons from short and long trajectories for the first rescattering time. The width of the rings is broader than other interference structures, which is quite different from the interference between the direct and the backward rescattering electrons as shown in Fig. 3(b).

In the case of the rescattering occurring at the second returning (type D, Fig. 1), the relationships between the final momentum and the initial momentum for forward-rescattering $\theta_0 = 0°$ and backward-rescattering $\theta_0 = \pi$ are shown in Fig. 4(b). Different from the type C, the final momenta of backward and forward rescattering electrons are all in $p_x > 0$ plane for type D. Same as type C, there are also two solutions of the initial momenta for the same final momentum which correspond to the short and long trajectories. The interference between the backward-rescattering electrons from these two different trajectories is shown in Fig. 4(d). It exhibits wide width
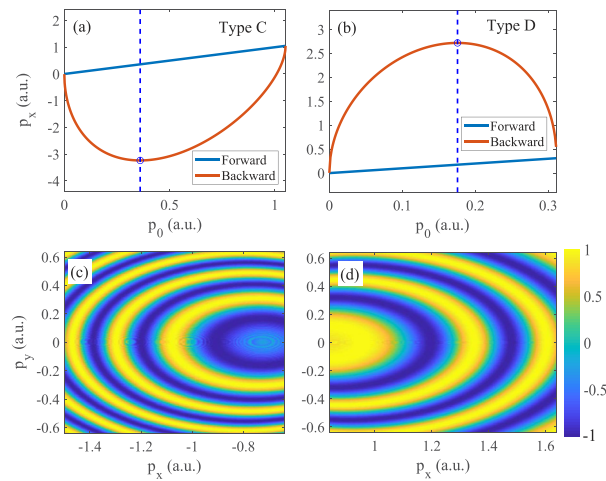
Fig. 4. (a) and (b) show the relationships between the final longitudinal momentum p_x and the initial momentum p_0 for the rescattering occurring at the first (type C, Fig. 1) and the second (type D, Fig. 1) returning. The blue and red lines correspond to the forward-rescattering ($\theta_0 = 0$) and backward-rescattering electrons ($\theta = \pi$), respectively. The dash lines separate the different initial momenta for the same final backward-rescattering momentum which correspond to the short and long trajectories. (c) and (d) show the interference between the backward-rescattering electrons from short and long trajectories for the rescattering occurring at the first (type C) and the second (type D) returning.

semi-rings structure and is located at the $p_y > 0$ plane. Comparing this wide semi-rings structure with the interference structures labeled by VI in Fig. 2(b) indicates that the type VI structures originate from the interference between the backward-rescattering electrons from long and short trajectories for type D.

4. Control the interference structures in attosecond streaking

In Fig. 2, different types of interference are mixed in the PEMDs, which hinders us from extracting the information from these interference structures. Therefore, it is necessary to selectively enhance the specific type of interference. Here, we control these interference structures by changing the time delay between the SAP and the IR pulses. Due to the binding potential of H atom is close to the current experiment condition, we choose the H atom as an example to show this method. Figure 5 shows the PEMDs for the ionization of model H atom for different time delays. The center frequency of the SAP is 0.54 a.u. which is higher than the binding potential of target. The intensity of the IR pulse is 1×10^{13} W/cm^2 which is so weak that the ionization from the ground state by the IR field can be neglected. There are mainly two types of interference structures, i.e., the curved fringes located at the $p_x < 0$ and the spiderlike structure located at the $p_x > 0$. As analyzed in Sec. 3, the curved fringes are the backward-rescattering hologram and the spiderlike structure is the forward-rescattering hologram. Figures 5(a)–5(d) show that the backward-rescattering photoelectron hologram is suppressed and the forward-scattering holography is enhanced as the time delay τ between the SAP and the IR field increases. For instance, the backward-rescattering hologram is distinct at $\tau = 0$, as shown in Fig. 5(a). Whereas, there is only the forward-rescattering hologram in Fig. 5(d) at $\tau = T_1/4$. This clear interference pattern can be used to retrieve the information of the atoms and electrons.
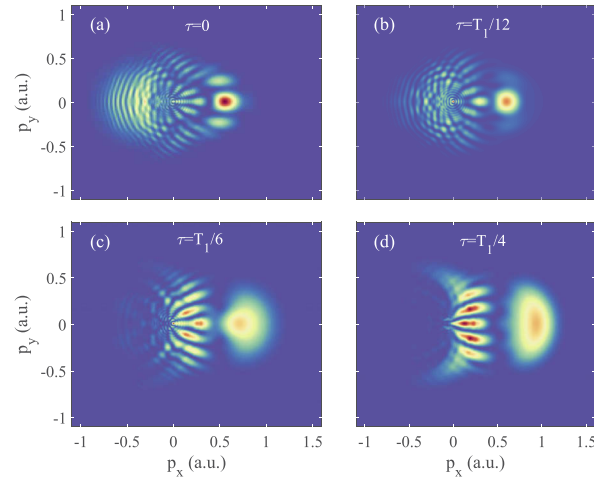
Fig. 5. The PEMDs in the log scale for the ionization of the H atom by linearly polarized SAP in a linearly polarized IR field. The time delays τ between the SAP and the IR field for (a)-(d) are 0, $T_1/12$, $T_1/6$ and $T_1/4$, respectively. Here, T_1 is the optical cycle of the IR field. The intensities of the 1600-nm IR field and the SAP are 1×10^{13} W/cm^2 and 2×10^{14} W/cm^2, respectively. The center frequency of the SAP is 0.54 a.u.. The SAP and IR field are both polarized along x−axis.

5. Retrieve the phase of the electron wave packets

Here, as an example of the application of the interference structures, we show that the phase of the EWPs ionized by the SAP can be extracted by these interference structures. In pervious works, the phase of the continuous EWPs ionized by the linearly polarized SAP has been extracted by the attosecond streaking technique [24,25]. In this section, we show the phase of the EWPs ionized by the linearly polarized as well as the circularly polarized SAP can be exacted by the forward-rescattering holography.

Figure 6 shows the PEMDs for ionization of model H atom by the linearly and circularly polarized SAP. For the linearly polarized SAP, the PEMDs reveal a two-lobe structure along the polarization direction of the SAP. For instance, when the angle between polarization direction and x−axis is $\pi/3$, the lobes distribute along the line of $\alpha = \pi/3$ as shown in Fig. 6(b). Here α is the angle between the direction of final momentum and x−axis. Figures 6(c) and 6(d) are the PEMDs for the right-hand and left-hand circularly polarized SAP, respectively. The PEMDs exhibit a ring structure with a momentum radius $p = \sqrt{p_x^2 + p_y^2} = \sqrt{2(\omega_2 - I_p)}$. These structures are the characteristic feature of single-photon ionization. The amplitude for a single photon ionization $M(\mathbf{p})$ can be expressed in the dipole form as

$$M(\mathbf{p}) = \langle \psi_c \mathbf{r} \cdot \mathbf{E} | \psi_0 \rangle = |M(\mathbf{p})| e^{i\phi}, \tag{17}$$

where ψ_0 and ψ_c are the initial and final states, respectively. ϕ is the phase of the continuous EWPs. In strong-field approximation (SFA), where the final state is the Volkov state, this phase is just the phase of the corresponding spherical harmonics, as shown in Fig. 7. For the linearly polarized SAP, there is phase jump of π between the two lobes, as shown in Fig. 7(a). For the circularly polarized SAP, ϕ is linear to α, i.e., $\phi = \pm\alpha$, where $-$ and $+$ correspond to the right-hand and left-hand circularly polarized SAP, respectively, as shown in Fig. 7(b). As a preliminary demonstration, in the following we will show how this phase is expressed in the interference patterns of the PEMDs and the retrieval of this phase.
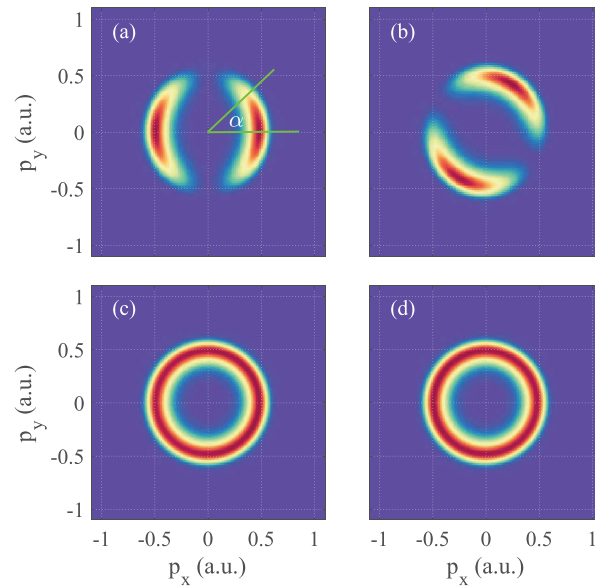
Fig. 6. The PEMDs for ionization of the model H atom by SAP. (a) and (b) are the PEMDs for the linearly polarized SAP. The angles between the x−axis and the polarization direction of SAP are 0 and $\pi/3$ for (a) and (b). (c) and (d) are the PEMDs for the right-hand circularly and left-hand circularly polarized SAP, respectively. The center frequency and the intensity of SAP are 0.54 a.u. and 2×10^{14} W/cm^2. α is the angle between the direction of the electric final momentum and x−axis.
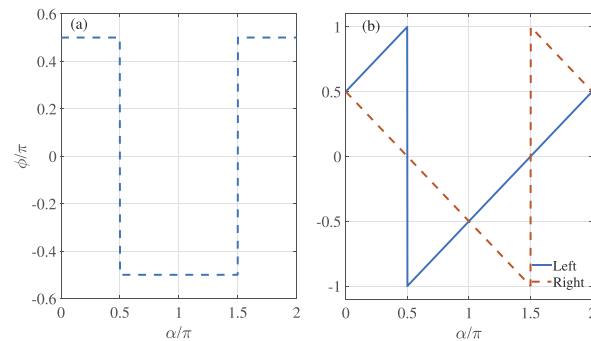

Fig. 7. The phase of the continuous electric wave packet calculated by SFA. α is the angle between the direction of the final momentum and x−axis as shown in Fig. 6(a). ϕ is the phase of the continuous EWPs ionized by the SAP which is calculated by SFA. (a) is the relationship of the phase of the initial EWPs and the direction of the final momentum for the linearly polarized SAP. (b) is the relationship for circularly polarized SAP. The blue solid and red dotted lines correspond to the left-hand and right-hand circularly polarized SAP, respectively.

To show the phase jump between the two lobes ionized by the linearly polarized SAP, we employ an IR field to induce interferences in the PEMD. The IR field is polarized along x−axis and we change the polarization direction of the SAP. Figure 8 shows the PEMDs for different polarization directions θ of the SAP. The near-forward rescattering holographic interference structure is clearly visible in the PEMDs. As explained in Sec. 2.2, the phase difference between the direct and the near forward rescattering electrons along the trajectories is $\frac{1}{2}p_y^2(t_s - t_0)$ [45,65],

where t_0 and t_s are the ionization and rescattering times, respectively. This phase difference could qualitatively reproduce the overall shape of the interference pattern, while it fails in quantitative level. In our pervious study, we have demonstrate that the exact phase difference could be written as [51]

$$\delta\phi = \frac{1}{2}p_y^2(t_s - t_0) + \phi_s + [\phi(0; t_0) - \phi(p_y; t_0)], \tag{18}$$

where the first term is the same as that given by the semiclassical model. The second term accounts for the phase due to the interaction of the rescattering electron with the parent ion during the rescattering process. This term has been revealed in our pervious paper [50]. The third term relates to the phases of the continuous EWPs ionize by SAP.
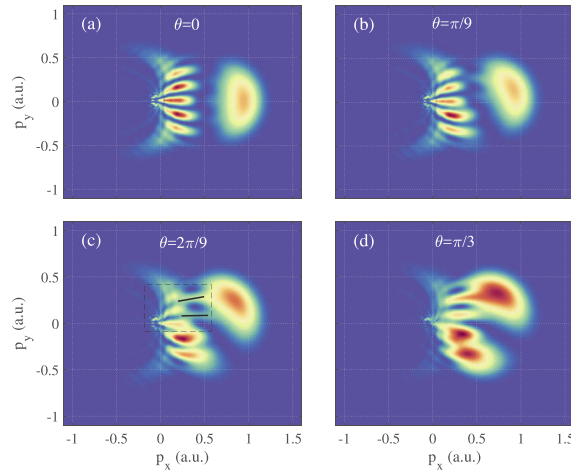

Fig. 8. The PEMDs from ionization of H atom by a linearly polarized SAP in a linearly polarized IR field. The angles between the polarization direction of SAP and $x-$axis in (a)-(d) are 0, $\pi/9$, $2\pi/9$ and $\pi/3$, respectively. The IR field is polarized at $x-$axis. The intensity of the 1600-nm IR field and the SAP is 1×10^{13} W/cm^2 and 2×10^{14} W/cm^2, respectively. The center frequency of the SAP is 0.54 a.u.. The PEMD in black dotted box shows the interference minima change to the interference maxima.

In Figs. 8(a) and 8(b), the positions of the interference maxima and minima are exactly symmetric about $p_y = 0$. In these cases, the direct and the forward-rescattering electrons are from the same lobe. As θ increases, the interference minima change to the interference maxima as shown in the black dotted box in Fig. 8(c). The interference maximum at $p_y = 0$ changes into a minimum for $\theta = \pi/3$, as shown in Fig. 8(d). In this case, the direct and the forward-rescattering electrons originate from different lobes ionized by the linear polarization SAP. The change of the interference maxima to the minima of the interference structures means $\phi(0; t_0) - \phi(p_y; t_0)$ changing from 0 to π, which indicates that there is a phase jump of π between the two lobes.

Figure 9 shows the PEMD for the ionization of H atom by the right-hand circularly polarized SAP in a linearly polarized IR field. The positions of the interference minima and maxima in the hologram are obviously asymmetric with respect to $p_y = 0$. Figure 10(a) shows the PEMD at $p_x = 0.3$ a.u. and the results of the linearly polarized SAP are also presented for comparison. We fit the cuts by the function

$$e^{-f(p_y)}[1 + g(p_y)cos\delta\phi]. \tag{19}$$

Here, $f(p_y)$ describes the background contribution and is determined by fitting the logarithm of the PMD by a polynomial. Dividing the fitted function by $e^{-f(p_y)}$, we obtain an oscillating function with a smooth envelope $g(p_y)$, which is again fitted by a polynomial. By construction,

the remaining factor $\cos\delta\phi$ is bounded between -1 and $+1$ which is shown in Fig. 10(b). More details of this phase extraction procedure were given in our pervious paper [51]. The shift of the positions of the minima and maxima of the circularly polarized SAP is visible. To retrieve the phase of continuous EWPs from the hologram, we extract the phase differences $\delta\phi_\pm$ from the PEMDs, as shown in Fig. 10(c). Here, $\delta\phi_\pm$ denote $\delta\phi(p_y)$ for $p_y>0$ and $p_y<0$, respectively. As discussed in our pervious work [52], the first and second terms in Eq. (18) for $p_y>0$ and $p_y<0$ exactly equal due to the symmetry of our system. Thus these terms can be eliminated by
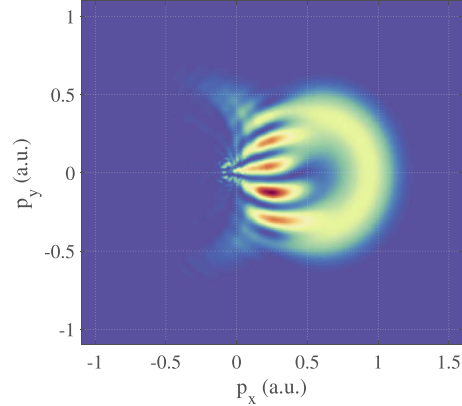

Fig. 9. The PEMD from ionization of H atom by the right-hand circularly polarized SAP in an IR field linearly polarized along x−axis. The intensity of the 1600-nm IR field and the SAP is 1×10^{13} W/cm^2 and 2×10^{14} W/cm^2, respectively. The center frequency of the SAP is 0.54 a.u..
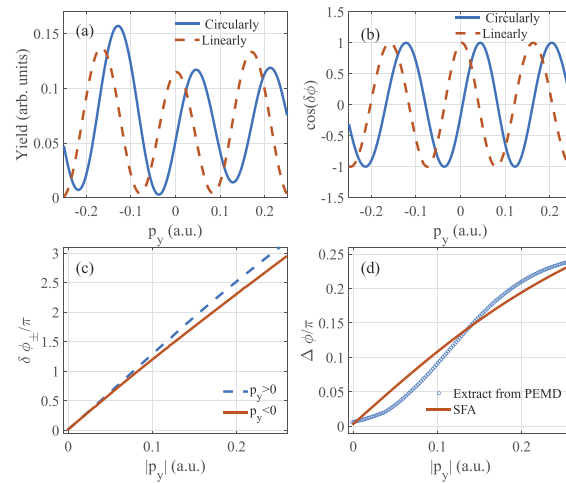

Fig. 10. Analysis of the forward-rescattering hologram in right-hand circularly polarized SAP. (a) Cuts of the PEMDs at $p_x = 0.3$ a.u. from Fig. 9 (right hand circularly polarized SAP) and Fig. 8(a) (linearly polarized SAP), as presented by the blue solid and red dashed lines, respectively. (b) The interference term $\cos\delta\phi$ extracted from the cuts in (a). (c) The phase difference $\delta\phi_{+,-}$ for $p_y>0$ (blue dash line) and $p_y<0$ (red solid line) obtained from the cuts in (a). (d) The phase difference $\Delta\phi = \delta\phi_+ - \delta\phi_-$ as a function of $|p_y|$ extracted from (a) (the blue circle line) and calculated by SFA (the red solid line), respectively.

performing a subtracting procedure

$$\Delta\phi = \delta\phi_+ - \delta\phi_- = \phi(-|p_y|) - \phi(|p_y|). \tag{20}$$

The result extracted from PEMDs is shown by the blue circle line in Fig. 10(d). For the atomic system studied here, this phase $\Delta\phi$ should be exactly the same as that in SFA, i.e, the one calculated from the corresponding spherical harmonics, which is shown by the red solid line in Fig. 10(d). It shows that the result extracted from the PEMDs agrees well with SFA, which indicates that the phase of the continuous EWPs ionized by the SAP can be extracted from the near-forward hologram. The small difference between the retrieved results and the phase of the spherical harmonic is due to our procedure of phase extraction. It can be improved in the future study on retrieving more meaningful phase of the continuous electron wave packets.

6. Conclusions

In conclusion, we have studied the low energy interference structures in attosecond streaking scheme. Different from the high-energy attosecond streaking, the PEMDs calculated by numerically solving the TDSE contain rich interference structures. The originations of different types of interference structures are identified with the semiclassical model. Moreover, we show that these interference structures can be controlled by changing the time delay between the SAP and the IR pulse. As an example of the application of the interference structures in attosecond streaking, we show that the phase of the continuous EWPs ionized by the linearly and circularly polarized SAP can be retrieved from the forward-rescattering hologram. Though for the atomic system studied here, the retrieved phase is just the phase of the spherical harmonics, the concept of our scheme could be applied to retrieve more meaningful phase of the ionized electron wave packet in more complex systems. We should mention that the developed experiment technique, such as atto-COLTRIMS [69], is capable of detecting these interference structures of the low energy photoelectron streaking.

Disclosures

The authors declare no conflicts of interest.

References

1. F. Quere, J. Itatani, G. L. Yudin, and P. B. Corkum, "Attosecond Spectral Shearing Interferometry," Phys. Rev. Lett. **90**(7), 073902 (2003).
2. R. Kienberger, E. Goulielmakis, M. Uiberacker, A. Baltuska, V. Yakovlev, F. Bammer, A. Scrinzi, Th. Westerwalbesloh, U. Kleineberg, U. Heinzmann, M. Drescher, and F. Krausz, "Atomic transient recorder," Nature **427**(6977), 817–821 (2004).
3. E. Goulielmakis, M. Uiberacker, R. Kienberger, A. Baltuska, V. Yakovlev, A. Scrinzi, Th. Westerwalbesloh, U. Kleineberg, U. Heinzmann, M. Drescher, and F. Krausz, "Direct Measurement of Light Waves," Science **305**(5688), 1267–1269 (2004).
4. M. Schultze, M. Fiess, N. Karpowicz, J. Gagnon, M. Korbman, T. Mercouris, C. A. Nicolaides, R. Pazourek, S. Nagele, J. Feist, J. Burgdörfer, A. M. Azzeer, R. Ernstorfer, R. Kienberger, U. Kleineberg, E. Goulielmakis, F. Krausz, and V. S. Yakovlev, "Delay in Photoemission," Science **328**(5986), 1658–1662 (2010).
5. A. S. Kheifets and I. A. Ivanov, "Delay in Atomic Photoionization," Phys. Rev. Lett. **105**(23), 233002 (2010).

6. J. C. Baggesen and L. B. Madsen, "Polarization Effects in Attosecond Photoelectron Spectroscopy," Phys. Rev. Lett. **104**(4), 043602 (2010).

7. M. Ivanov and O. Smirnova, "How Accurate Is the Attosecond Streak Camera?" Phys. Rev. Lett. **107**(21), 213605 (2011).

8. C.-H. Zhang and U. Thumm, "Electron-ion interaction effects in attosecond time-resolved photoelectron spectra," Phys. Rev. A **82**(4), 043405 (2010).

9. R. Pazourek, J. Feist, S. Nagele, and J. Burgdörfer, "Attosecond Streaking of Correlated Two-Electron Transitions in Helium," Phys. Rev. Lett. **108**(16), 163001 (2012).

10. R. Pazourek, S. Nagele, and J. Burgdörfer, "Time-resolved photoemission on the attosecond scale: opportunities and challenges," Faraday Discuss. **163**, 353–376 (2013).

11. S. Nagele, R. Pazourek, J. Feist, K. Doblhoff-Dier, C. Lemell, K. Tókési, and J. Burgdörfer, "Time-resolved photoemission by attosecond streaking: extraction of time information," J. Phys. B **44**(8), 081001 (2011).

12. J. Su, H. Ni, A. Becker, and A. Jaroń-Becker, "Attosecond-streaking time delays: Finite-range property and comparison of classical and quantum approaches," Phys. Rev. A **89**(1), 013404 (2014).

13. I. A. Ivanov, A. S. Kheifets, and V. V. Serov, "Attosecond time-delay spectroscopy of the hydrogen molecule," Phys. Rev. A **86**(6), 063422 (2012).

14. G. Dixit, H. S. Chakraborty, and M.-A. Madjet, "Time Delay in the Recoiling Valence Photoemission of Ar Endohedrally Confined in C_{60}," Phys. Rev. Lett. **111**(20), 203003 (2013).

15. V. V. Serov, V. L. Derbov, and T. A. Sergeeva, "Interpretation of time delay in the ionization of two-center systems," Phys. Rev. A **87**(6), 063414 (2013).

16. C.-H. Zhang and U. Thumm, "Attosecond photoelectron spectroscopy of metal surfaces," Phys. Rev. Lett. **102**(12), 123601 (2009).

17. A. K. Kazansky and P. M. Echenique, "One-Electron Model for the Electronic Response of Metal Surfaces to Subfemtosecond Photoexcitation," Phys. Rev. Lett. **102**(17), 177401 (2009).

18. C. Lemell, B. Solleder, K. Tókési, and J. Burgdörfer, "Simulation of attosecond streaking of electrons emitted from a tungsten surface," Phys. Rev. A **79**(6), 062901 (2009).

19. Q. Liao and U. Thumm, "Attosecond Time-Resolved Photoelectron Dispersion and Photoemission Time Delays," Phys. Rev. Lett. **112**(2), 023602 (2014).

20. Q.-C. Ning, L.-Y. Peng, S.-N. Song, W.-C. Jiang, S. Nagele, R. Pazourek, J. Burgdörfer, and Q. Gong, "Attosecond streaking of Cohen-Fano interferences in the photoionization of H_2^+," Phys. Rev. A **90**(1), 013423 (2014).

21. M. Wickenhauser, J. Burgdörfer, F. Krausz, and M. Drescher, "Time Resolved Fano Resonances," Phys. Rev. Lett. **94**(2), 023002 (2005).

22. H. Wang, M. Chini, S. Chen, C.-H. Zhang, F. He, Y. Cheng, Y. Wu, U. Thumm, and Z. Chang, "Attosecond Time-Resolved Autoionization of Argon," Phys. Rev. Lett. **105**(14), 143002 (2010).

23. S. Gilbertson, M. Chini, X. Feng, S. Khan, Y. Wu, and Z. Chang, "Monitoring and Controlling the Electron Dynamics in Helium with Isolated Attosecond Pulses," Phys. Rev. Lett. **105**(26), 263003 (2010).

24. V. S. Yakovlev, J. Gagnon, N. Karpowicz, and F. Krausz, "Attosecond Streaking Enables the Measurement of Quantum Phase," Phys. Rev. Lett. **105**(7), 073001 (2010).

25. T. Remetter, P. Johnsson, J. Mauritsson, K. Varjú, Y. Ni, F. Lépine, E. Gustafsson, M. Kling, J. Khan, R. López-Martens, K. J. Schafer, M. J. J. Vrakking, and A. L'Huillier, "Attosecond electron wave packet interferometry," Nat. Phys. **2**(5), 323–326 (2006).

26. D. Kiesewetter, R. R. Jones, A. Camper, S. B. Schoun, P. Agostini, and L. F. DiMauro, "Probing electronic binding potentials with attosecond photoelectron wavepackets," Nat. Phys. **14**(1), 68–73 (2018).

27. P. B. Corkum, "Plasma perspective on strong field multiphoton ionization," Phys. Rev. Lett. **71**(13), 1994–1997 (1993).

28. F. Krausz and M. Ivanov, "Attosecond physics," Rev. Mod. Phys. **81**(1), 163–234 (2009).

29. J. Li, Q. Zhang, L. Li, X. Zhu, T. Huang, P. Lan, and P. Lu, "Orientation dependence of high-order harmonic generation in nanowire," Phys. Rev. A **99**(3), 033421 (2019).

30. Z. Yang, W. Cao, X. Chen, J. Zhang, Y. Mo, H. Xu, K. Mi, Q. Zhang, P. Lan, and P. Lu, "All-optical frequency resolved optical gating for isolated attosecond pulse reconstruction," arXiv:1911.06427.

31. B. Wang, L. He, Y. He, Y. Zhang, R. Shao, P. Lan, and P. Lu, "All-optical measurement of high-order fractional molecular echoes by high-order harmonic generation," Opt. Express **27**(21), 30172–30181 (2019).

32. J. Li, L. Li, Q. Zhang, X. Zhu, T. Huang, P. Lan, and P. Lu, "Channel-closing effects of electronic excitation in solids," Opt. Express **27**, 37224–37235 (2019).

33. G. G. Paulus, W. Nicklich, H. Xu, P. Lambropoulos, and H. Walther, "Plateau in above threshold ionization spectra," Phys. Rev. Lett. **72**(18), 2851–2854 (1994).

34. X. Huang, Q. Zhang, S. Xu, X. Fu, X. Han, W. Cao, and P. Lu, "Coulomb focusing in retrapped ionization with near-circularly polarized laser field," arXiv:1911.09805.

35. T. Weber, H. Giessen, M. Weckenbrock, G. Urbasch, A. Staudte, L. Spielberger, O. Jagutzki, V. Mergel, M. Vollmer, and R. Dörner, "Correlated electron emission in multiphoton double ionization," Nature **405**(6787), 658–661 (2000).

36. Y. Zhou, C. Huang, Q. Liao, and P. Lu, "Classical Simulations Including Electron Correlations for Sequential Double Ionization," Phys. Rev. Lett. **109**(5), 053004 (2012).

37. A. Tong, Q. Li, X. Ma, Y. Zhou, and P. Lu, "Internal collision induced strong-field nonsequential double ionization in molecules," Opt. Express **27**(5), 6415 (2019).
38. T. Nubbemeyer, K. Gorling, A. Saenz, U. Eichmann, and W. Sandner, "Strong-Field Tunneling without Ionization," Phys. Rev. Lett. **101**(23), 233001 (2008).
39. Y. Zhao, Y. Zhou, J. Liang, Z. Zeng, Q. Ke, Y. Liu, M. Li, and P. Lu, "Frustrated tunneling ionization in the elliptically polarized strong laser fields," Opt. Express **27**(15), 21689–21701 (2019).
40. P. M. Paul, E. S. Toma, P. Breger, G. Mullot, F. Augé, P. Balcou, H. G. Muller, and P. Agostini, "Observation of a Train of Attosecond Pulses from High Harmonic Generation," Science **292**(5522), 1689–1692 (2001).
41. G. Sansone, E. Benedetti, F. Calegari, C. Vozzi, L. Avaldi, R. Flammini, L. Poletto, P. Villoresi, C. Altucci, R. Velotta, S. Stagira, S. De Silvestri, and M. Nisoli, "Isolated Single-Cycle Attosecond Pulses," Science **314**(5798), 443–446 (2006).
42. E. Goulielmakis, M. Schultze, M. Hofstetter, V. S. Yakovlev, J. Gagnon, M. Uiberacker, A. L. Aquila, E. M. Gullikson, D. T. Attwood, R. Kienberger, F. Krausz, and U. Kleineberg, "Single-Cycle Nonlinear Optics," Science **320**(5883), 1614–1617 (2008).
43. J. Itatani, J. Levesque, D. Zeidler, H. Niikura, H. Pépin, J. C. Kieffer, P. B. Corkum, and D. M. Villeneuve, "Tomographic imaging of molecular orbitals," Nature **432**(7019), 867–871 (2004).
44. C. I. Blaga, J. Xu, A. D. DiChiara, E. Sistrunk, K. Zhang, P. Agostini, and T. A. Miller, "Imaging ultrafast molecular dynamics with laser-induced electron diffraction," Nature **483**(7388), 194–197 (2012).
45. Y. Huismans, A. Rouzée, A. Gijsbertsen, J. H. Jungmann, A. S. Smolkowska, P. S. W. M. Logman, F. Lépine, C. Cauchy, S. Zamith, T. Marchenko, J. M. Bakker, G. Berden, B. Redlich, A. F. G. van der Meer, H. G. Muller, W. Vermin, K. J. Schafer, M. Spanner, M. Y. Ivanov, O. Smirnova, D. Bauer, S. V. Popruzhenko, and M. J. J. Vrakking, "Time-Resolved Holography with Photoelectrons," Science **331**(6013), 61–64 (2011).
46. M. Meckel, A. Staudte, S. Patchkovskii, D. M. Villeneuve, P. B. Corkum, R. Dörner, and M. Spanner, "Signatures of the continuum electron phase in molecular strong-field photoelectron holography," Nat. Phys. **10**(8), 594–600 (2014).
47. D. D. Hickstein, P. Ranitovic, S. Witte, X.-M. Tong, Y. Huismans, P. Arpin, X. Zhou, K. Ellen Keister, C. W. Hogle, B. Zhang, C. Ding, P. Johnsson, and N. Toshima, "Direct Visualization of Laser-Driven Electron Multiple Scattering, and Tunneling Distance in Strong-Field Ionization," Phys. Rev. Lett. **109**(7), 073004 (2012).
48. Q. Ke, Y. Zhou, J. Tan, M. He, J. Liang, Y. Zhao, M. Li, and P. Lu, "Two-dimensional photoelectron holography in strong-field tunneling ionization by counter rotating two-color circularly polarized laser pulses," Opt. Express **27**, 32193–32209 (2019).
49. Y. Feng, M. Li, S. Luo, K. Lui, B. Du, Y. Zhou, and P. Lu, "Semiclassical analysis of photoelectron interference in a synthesized two-color laser pulses," Phys. Rev. A **100**(6), 063411 (2019).
50. Y. Zhou, O. I. Tolstikhin, and T. Morishita, "Near-Forward Rescattering Photoelectron Holography in Strong-Field Ionization: Extraction of the Phase of the Scattering Amplitude," Phys. Rev. Lett. **116**(17), 173001 (2016).
51. M. He, Y. Li, Y. Zhou, M. Li, W. Cao, and P. Lu, "Direct Visualization of Valence Electron Motion Using Strong-Field Photoelectron Holography," Phys. Rev. Lett. **120**(13), 133204 (2018).
52. J. Tan, Y. Zhou, M. He, Y. Chen, Q. Ke, J. Liang, X. Zhu, M. Li, and P. Lu, "Determination of the Ionization Time Using Attosecond Photoelectron Interferometry," Phys. Rev. Lett. **121**(25), 253203 (2018).
53. M. Li, H. Xie, W. Cao, S. Luo, J. Tan, Y. Feng, B. Du, W. Zhang, Y. Li, Q. Zhang, P. Lan, Y. Zhou, and P. Lu, "Photoelectron holographic interferometry to probe the longitudinal momentum offset at the tunnel exit," Phys. Rev. Lett. **122**(18), 183202 (2019).
54. S. Luo, M. Li, W. Xie, K. Liu, Y. Feng, B. Du, Y. Zhou, and P. Lu, "Exit momentum, and instantaneous ionization rate of nonadiabatic tunneling ionization in elliptically polarized laser fields," Phys. Rev. A **99**(5), 053422 (2019).
55. W. Xie, M. Li, S. Luo, M. He, K. Liu, Q. Zhang, Y. Zhou, and P. Lu, "Nonadiabaticity-induced ionization time shift in strong-field tunneling ionization," Phys. Rev. A **100**(2), 023414 (2019).
56. J. Mauritsson, P. Johnsson, E. Mansten, M. Swoboda, T. Ruchon, A. L'Huillier, and K. J. Schafer, "Coherent Electron Scattering Captured by an Attosecond Quantum Stroboscope," Phys. Rev. Lett. **100**(7), 073003 (2008).
57. M.-H. Xu, L.-Y. Peng, Z. Zhang, Q. Gong, X.-M. Tong, E. A. Pronin, and A. F. Starace, "Attosecond Streaking in the Low-Energy Region as a Probe of Rescattering," Phys. Rev. Lett. **107**(18), 183001 (2011).
58. J.-W. Geng, L.-Y. Peng, S.-N. Song, and Q. Gong, "Interference structures in photoelectron spectra of atoms ionized by XUV pulses in the presence of a strong IR field," Phys. Rev. A **88**(5), 053418 (2013).
59. X. Yu, M. Li, M. Han, and Y. Liu, "Controlling backward-scattering photoelectron holography by attosecond streaking," Phys. Rev. A **98**(1), 013415 (2018).
60. J. Tan, Y. Zhou, M. He, Q. Ke, J. Liang, Y. Li, M. Li, and P. Lu, "Time-resolving tunneling ionization via strong-field photoelectron holography," Phys. Rev. A **99**(3), 033402 (2019).
61. Y. Liu, J. Tan, M. He, H. Xie, Y. Qin, Y. Zhao, M. Li, Y. Zhou, and P. Lu, "Photoelectron holographic interferences from multiple returning in strong-field tunneling ionization," Opt. Quantum Electron. **51**(5), 145 (2019).
62. M. R. Hermann and J. A. Fleck, "Split-operator spectral method for solving the time-dependent Schrödinger equation in spherical coordinates," Phys. Rev. A **38**(12), 6000–6012 (1988).
63. M. Protopapas, C. H. Keitel, and P. L. Knight, "Atomic physics with super-high intensity lasers," Rep. Prog. Phys. **60**(4), 389–486 (1997).
64. M. Li, J. Yuan, X. Sun, J. Yu, Q. Gong, and Y. Liu, "Recollision-induced subcycle interference of molecules in strong laser fields," Phys. Rev. A **89**(3), 033425 (2014).

65. X.-B. Bian, Y. Huismans, O. Smirnova, K.-J. Yuan, M. J. J. Vrakking, and A. D. Bandrauk, "Subcycle interference dynamics of time-resolved photoelectron holography with midinfrared laser pulses," Phys. Rev. A **84**(4), 043420 (2011).
66. D. G. Arbó, K. L. Ishikawa, K. Schiessl, E. Persson, and J. Burgdörfer, "Intracycle, and intercycle interferences in above-threshold ionization: The time grating," Phys. Rev. A **81**(2), 021403 (2010).
67. X.-B. Bian and A. D. Bandrauk, "Orientation-dependent forward-backward photoelectron holography from asymmetric molecules," Phys. Rev. A **89**(3), 033423 (2014).
68. C. Liu, M. Reduzzi, A. Trabattoni, A. Sunilkumar, A. Dubrouil, F. Calegari, M. Nisoli, and G. Sansone, "Carrier-Envelope Phase Effects of a Single Attosecond Pulse in Two-Color Photoionization," Phys. Rev. Lett. **111**(12), 123901 (2013).
69. J. Vos, L. Cattaneo, S. Patchkovskii, T. Zimmermann, C. Cirelli, M. Lucchini, A. Kheifets, A. S. Landsman, and U. Keller, "Orientation-dependent stereo Wigner time delay, and electron localization in a small molecule," Science **360**(6395), 1326–1330 (2018).